

Crystallization behavior of nano-composite based on poly(vinylidene fluoride) and organically modified layered titanate

Kumiko Asai^a, Masami Okamoto^{a,*}, Kohji Tashiro^b

^aAdvanced Polymeric Nanostructured Materials Engineering, Graduate School of Engineering, Toyota Technological Institute, 2-12-1 Hisakata, Tempaku, Nagoya 468 8511, Japan

^bDepartment of Future Industry-Oriented Basic Science and Materials, Graduate School of Engineering, Toyota Technological Institute, 2-12-1 Hisakata, Tempaku, Nagoya 468 8511, Japan

ARTICLE INFO

Article history:

Received 29 February 2008

Received in revised form 4 July 2008

Accepted 19 July 2008

Available online 29 July 2008

Keywords:

Poly(vinylidene fluoride)

Nano-composites

Crystallization

ABSTRACT

To understand the effect of the nano-filler particles on the crystallization kinetics and crystalline structure of poly(vinylidene fluoride) (PVDF) upon nano-composite formation, we have prepared PVDF/organically modified layered titanate nano-composite via melt intercalation technique. The layer titanate (HTO) is a new nano-filler having highly surface charge density compared with conventional layered silicates. The detailed crystallization behavior and its kinetics including the conformational changes of the PVDF chain segment during crystallization of neat PVDF and HTO-based nano-composite (PVDF/HTO) have been investigated by using differential scanning calorimetric, wide-angle X-ray diffraction, light scattering, and infrared spectroscopic analyses. The neat PVDF predominantly formed α -phase in the crystallization temperature range of 110–150 °C. On the other hand, PVDF/HTO exhibited mainly α -phase crystal coexisting with γ - and β -phases at low T_c range (110–135 °C). A major γ -phase crystal coexists with β - and α -phases appeared at high T_c (=140–150 °C), owing to the dispersed layer titanate particles as a nucleating agent. The overall crystallization rate and crystalline structure of pure PVDF were strongly influenced in the presence of layered titanate particles.

© 2008 Elsevier Ltd. All rights reserved.

1. Introduction

Over the last few years, the utility of inorganic nanoscale particles as filler to enhance the polymer performance has been established. Of particular interest is recently developed nano-composite technology consisting of a polymer and organically modified layered filler (organo-clay) because they often exhibit remarkably improved mechanical and various other materials' properties as compared with those of virgin polymer or conventional composite (micro/macro-composites) [1–5]. These concurrent property improvements are well beyond what can be generally achieved through the micro/macro-composites' preparation.

The effect of organo-clay on the crystal structure and polymorphism of the matrix semi-crystalline polymer has been investigated in nano-composites. The crystallization rate of nylon 6 was enhanced dramatically in the presence of clay particles as revealed from light scattering experiments [6]. Nylon 6 was crystallized extensively in the γ -form in the nano-composite because of the epitaxial crystallization, which was also revealed from the

transmission electron microscopic images. Mathias et al. [7] have investigated nylon 6 nano-composite using ¹⁵N nuclear magnetic resonance and concluded that the clay stabilizes the γ -phase of nylon 6.

A new polymorph of poly(vinylidene fluoride) (PVDF) was introduced in PVDF-based nano-composites [8–11]. The phase is preferentially crystallized in the β polymorph in the presence of the organically modified clay (organo-clay). They reported that similar crystal lattices between clay and the β polymorph, and the large flat surface of the clay are the key factors to interact between polymer and inorganic materials [11]. Recently, a full analysis of the crystallization of PVDF in nano-composites has been done by Dillon et al. [12,13]. Using Fourier transform infrared spectroscopy (FTIR), they reported that α -form coexists with β - and γ -phases, and the amount of β -phase increases with increasing clay content.

The interaction of an inorganic phase of the organo-clay with the semi-crystalline polymer, the loading amount of the interface, shape, dimension, and surface properties of the layered filler can potentially change the crystallization kinetics and the crystalline morphology of the matrix polymer [14–16].

Despite extensive studies of the polymer crystallization in nano-composite systems, the mechanism underlying of the different polymorphisms is not very well explored in the literature.

* Corresponding author. Tel.: +81 52 809 1861; fax: +81 52 809 1864.
E-mail address: okamoto@toyota-ti.ac.jp (M. Okamoto).

To prove the effect of the nano-filler particles on the crystallization kinetics and crystalline structure of PVDF upon nano-composite formation, we have to choose another type of organically modified layered fillers (OMLFs) having different charge densities and different crystal lattice parameters [17,18].

In this regard, we expect that the crystallization behavior of the PVDF/organically modified layered titanate nano-composites should be different from the behavior of PVDF/organo-clay nano-composite. Therefore, we have attempted in this work to prepare PVDF/organically modified layered titanate nano-composite via melt intercalation technique and then investigated the crystallization behavior including the conformational changes of the PVDF chain segment of the nano-composite during crystallization. Knowledge of such a comparison should also be useful in assessing how does the nano-filler control the crystallization behavior and the different polymorphisms of PVDF matrix in the layered titanate-based nano-composites?

2. Experimental section

2.1. Materials

A poly(vinylidene fluoride) (PVDF) fine powder ($M_n = 5.34 \times 10^5$ g/mol, $T_g \sim -40$ °C and $T_m = \sim 158$ °C) purchased from Aldrich, was used as a polymer matrix. The layer titanate (HTO) is a new nano-filler having highly surface charge density [18] compared with conventional layered silicates (synthetic fluorine hectorite (*syn-FH*) and montmorillonite (MMT)). Their names and chemical formulae, and designations (as written in the text) are presented in Table 1.

The surface charge density is particularly important because it determines the interlayer structure of intercalants as well as cation exchange capacity (CEC). The characterizing method consists of total elemental analysis and the dimension of the unit cell [18]:

$$\text{Surface charge} : e^-/\text{nm}^2 = \zeta/ab \quad (1)$$

where ζ is the layer charge (1.07 for HTO, 0.66 for *syn-FH* and 0.33 for MMT). a and b are cell parameters of HTO ($a = 3.782$ Å, $b = 2.978$ Å [18]), *syn-FH* ($a = 5.24$ Å, $b = 9.08$ Å [18]), and MMT ($a = 5.18$ Å, $b = 9.00$ Å [18]). For *syn-FH*, however, about 30% of the interlayer Na^+ ions are not replaced quantitatively by intercalants due to the non-active for ion-exchange reactions [18]. For HTO, only 27% of interlayer H^+ (H_3O^+) is active for ion-exchange reactions. The remaining part is the non-active sites in the HTO. Thus the incomplete replacement of the interlayer ions is ascribed to the intrinsic chemical reactivity. The characteristic parameters of the nano-fillers are also summarized in Table 1. HTO has highly surface charge density of $1.26e^-/\text{nm}^2$ compared with those of *syn-FH* ($0.971e^-/\text{nm}^2$) and MMT ($0.780e^-/\text{nm}^2$). From these results, we can estimate the average distance between exchange sites, which is calculated to be 0.888 nm for HTO, 1.014 nm for *syn-FH* and 1.188 nm for MMT, respectively. This estimation assumes that the

cations are evenly distributed in a cubic array over the nano-filler surface and that half of the cations are located on the one side of the platelet and the other half reside on the other side.

For comparison, the four different types of OMLF having different types of intercalants and different fillers used in this study were synthesized by replacing Na^+ and K^+ ions in different nano-fillers with alkylammonium cations (i.e., octadecyl tri-methylammonium (C_{18}TM), di-octadecyl di-methylammonium (DC_{18}DM) cations) [18–20] (see Table 2).

2.2. Nano-composites preparation

OMLFs (powder) and PVDF (fine powder) were first dry-mixed by shaking them in a bag. Melt mixing was carried out in a miniature mixer of gram-scale, Mini-MAX Molder (CS-183, Custom Scientific Instruments Inc.) operated at 190 °C for 4 min to yield intercalated PVDF-based nano-composite strands. The extruded strands were then converted into sheets with a thickness of 0.3–0.5 mm by pressing with ≈ 1 MPa at 190 °C for 30 s using a hot press. The OMLF content in all PVDF-based nano-composites was 5 wt%.

2.3. Crystallization

The molded sheets were again annealed at 200 °C for 3 min, and then they were quickly transferred into a hot stage set at the desired crystallization temperature (T_c) ($=130$ and 150 °C) and crystallized until full solidification (confirmed from the kinetics of crystallization using a polarizing optical microscope (POM)). The crystallized specimens were characterized by using differential scanning calorimeter (DSC), wide-angle X-ray diffraction (WAXD) and transmission electron microscope (TEM).

2.4. Differential scanning calorimetry (DSC)

The crystallized specimens were characterized by using temperature-modulated DSC (TA 2920; TA Instruments) at the heating rate of 5 °C/min with a heating/cooling cycle of the modulation period of 60 s and an amplitude of ± 0.769 °C, to determine the crystallization temperature with cooling from melt (T_{cc}), the melting temperature (T_m) and heat of fusion (ΔH_f); the DSC was calibrated with Indium before experiments. For the measurement of degree of crystallinity (χ_c) prior to DSC analysis, the extra heat absorbed by the crystallites formed during heating had to be subtracted from the total endothermic heat flow due to the melting of the whole crystallites. This can be done according to the principles and procedures described in our previous paper [21]. By considering the melting enthalpy of 100% crystalline PVDF as 104.6 J/g [22], we have estimated the value of the χ_c of neat PVDF and PVDF-based nano-composites, and these values are also presented in Table 3.

Table 1
Characteristic parameters of nano-fillers

Parameters	HTO	<i>syn-FH</i>	MMT
Chemical formula	$\text{H}_{1.07}\text{Ti}_{1.73}\text{O}_{3.95} \cdot 0.5\text{H}_2\text{O}$	$\text{Na}_{0.66}\text{Mg}_{2.6}\text{Si}_4\text{O}_{10}(\text{F})_2$	$\text{Na}_{0.33}(\text{Al}_{1.67}\text{Mg}_{0.33})\text{Si}_4\text{O}_{10}(\text{OH})_2$
Particle size/nm	~ 100 – 200	~ 100 – 200	~ 100 – 200
BET area/m ² /g	~ 2400	~ 800	~ 700
CEC ^a /meq/100 g	~ 200 (660)	~ 120 (170)	~ 90 (90)
$e^-/\text{charge}/\text{nm}^2$	1.26	0.971	0.708
Density/g/cm ³	2.40	2.50	2.50
Refractive index (n_D^{20})	2.3	1.55	1.55
pH	4–6	9–11	7.5–10

^a Methylene blue adsorption method. The values in the parenthesis are calculated from chemical formula of nano-fillers.

Table 2
Name, chemical formula and designation of the OMLF used

Name, formula and designation	Nano-fillers and designation	Code
[(CH ₃) ₃ N (C ₁₈ H ₃₇) ⁺ Cl ⁻ octadecyl tri-methylammonium chloride, (C ₁₈ TM)]	Montmorillonite (MMT)	MMT-C ₁₈ TM
	Synthetic fluorine hectorite (<i>syn</i> -FH)	HTO-C ₁₈ TM
[(CH ₃) ₂ N (C ₁₈ H ₃₇) ⁺ Cl ⁻ , di-octadecyl di-methylammonium chloride, (DC ₁₈ DM)]	Layered titanate (HTO)	MMT-DC ₁₈ DM
		<i>syn</i> -FH-DC ₁₈ DM

2.5. Wide-angle X-ray diffraction (WAXD)

WAXD analyses were performed for the OMLF powders, neat PVDF and each nano-composite using an Mxlabo X-ray diffractometer (MAC Science Co.; 3 kW, graphite monochromator, Cu K α radiation ($\lambda_x = 0.154$ nm), operated at 40 kV and 20 mA). Samples were scanned in fixed time mode with counting time of 2 s at room temperature under diffraction angle 2θ in the range of 1° – 30° .

2.6. Transmission electron microscopy (TEM)

Nanoscale structure of PVDF-based nano-composites was investigated by means of TEM (H-7100, Hitachi Co.), operating at an accelerating voltage of 100 kV. The ultra thin sections (the edge of the sample sheet perpendicular to the compression mold) with a thickness of 100 nm were microtomed at -80°C using a Reichert Ultra cut cryo-ultramicrotome without staining. TEM photographs were taken from the edge of the compression molded sheets. To investigate the micro-scale morphology of the nano-composites, we also used polarizing optical microscope (POM). Because TEM micrograph covers a small area, this might not be entirely representative for the overall microstructure of the sample. The molded sheets were first sandwiched between two pieces of cover glass and placed on a laboratory hot plate at above T_m of PVDF for 30 s. The molten film was then rapidly put on a thermostated hot stage (200°C) (Linkam RTVMS, Linkam Scientific Instruments, Ltd.) mounted on a POM (Nikon OPTIPHOTO2-POL) [19].

2.7. Rayleigh scattering photometry

We have employed time-resolved light scattering (LS) photometry to estimate the overall crystallization rate and its kinetics in the supercooled state of neat PVDF and nano-composites. The thin sample of about $150\ \mu\text{m}$ thickness was quickly transferred from the melt state ($\sim 200^\circ\text{C}$ for 3 min in order to remove the thermal history) to the Linkam hot stage, placed in the

LS apparatus, set at the predetermined temperature, and immediately after attaining the T_c , a time-resolved LS measurement was carried out in the temperature range of 100 – 153°C in the supercooled state under the quiescent state. It should be mentioned here that there was some time lag between putting the sample on hot stage and to switch on the computer to collect the data which is ~ 1 s, sufficient for the equilibration of temperature. The one-dimensional photometer was equipped with a 38-channel photodiode (PDA: Hamamatsu Photonics Co.) array, which facilitated the angular dependence of scattering angle (θ_{LS}) was covered between 1.4° and 30° . The radiation of polarized He–Ne laser of 632.8 nm wavelengths was used vertically to the sample, and the scattering profile was observed at an azimuthal angle of 45° under H_V (cross-polarized) alignment. We also used a conventional Polaroid camera (camera length = 100 – 400 mm, which gave a scattering vector range of 0.37 – $4.15\ \mu\text{m}^{-1}$) to recover the scattering patterns on a photographic film (Fuji FP-100B; ISO = 100) with an exposure time of $1/250$ s [23]. The photographs were taken after full solidification of the sample.

2.8. Fourier transform infrared spectroscopy (FTIR)

FTIR spectra were collected at $2\ \text{cm}^{-1}$ nominal resolution using a Varian FTS7000 spectrometer equipped with a MCT detector in transmission mode. The spectra were obtained by averaging 32 scans with a mean collection length of 1 s per spectrum. The background spectra used for reduction were collected at the same T_c with the sample. The homogenous mixture of KBr powder and PVDF (fine powder) or PVDF-based nano-composites (powder) in the weight ratio 95:5 was prepared. The mixtures were then converted into disks with a thickness of ~ 0.4 mm by pressing. The disks were placed in a homemade environmental heating chamber, which allowed to reach the desired T_c in a very short time (~ 2 s). Each sample was kept at 200°C for 3 min to erase any thermal history, and it was immediately cooled to T_c . After attaining the T_c , a time-resolved FTIR measurement was carried out in the temperature range of 110 – 150°C . The collected data were processed by soft ware (Grams/AI[®], Thermo Galactic Co., USA).

Table 3
DSC properties of neat PVDF and its nano-composites

Sample	$T_c/^\circ\text{C}$	$T_m/^\circ\text{C}$	$T_{cc}/^\circ\text{C}$	$\Delta H_f/\text{J/g}$	$X_c/\%$
PVDF	100	158.48	128.05	49.93	47.73
	130	157.37	127.88	62.58	59.83
	150	160.65	127.83	56.95	54.45
PVDF/MMT-C ₁₈ TM	100	161.04	142.66	55.2	55.55
	130	162.83	143.14	48.32	48.63
	150	166.67	143.04	54.45	54.80
PVDF/MMT-DC ₁₈ DM	100	161.78	142.7	51.00	51.32
	130	162.86	143.06	49.88	50.20
	150	166.87	143.15	52.62	52.95
PVDF/HTO-C ₁₈ TM	100	156.81	136.06	53.34	53.68
	130	157.69	139.37	58.98	59.35
	150	168.23	138.52	59.12	59.49
PVDF/ <i>syn</i> -FH-DC ₁₈ DM	100	159.53	141.13	41.22	41.48
	130	163.62	141.42	42.87	43.14
	150	166.65	141.31	47.61	47.91

3. Results and discussion

3.1. PVDF-based nano-composites formation

To elucidate the morphologies after preparation of the nano-composites, we conducted POM observation at 200°C . PVDF does not contribute to the measured film birefringence because of melting. However, MMT platelets could contribute to the negative birefringence because the refractive index value normal to the basal plane (001) ($n_{\text{out-of-plane}} = 1.485$) is smaller than the basal-plane (in-plane) refractive index values ($n_{\text{in-plane}} = 1.505$ – 1.550) [24].

Fig. 1 shows the morphologies of PVDF-based nano-composites. The OMLF content in all nano-composites was 5 wt%. It is clear from the POM photographs that stacked-and-agglomerated structure of layers is evident in MMT-based nano-composites (PVDF/MMTs), while good dispersion appears in PVDF/*syn*-FH-DC₁₈DM. For PVDF/HTO-C₁₈TM, we still observe large stacked titanate layers in the

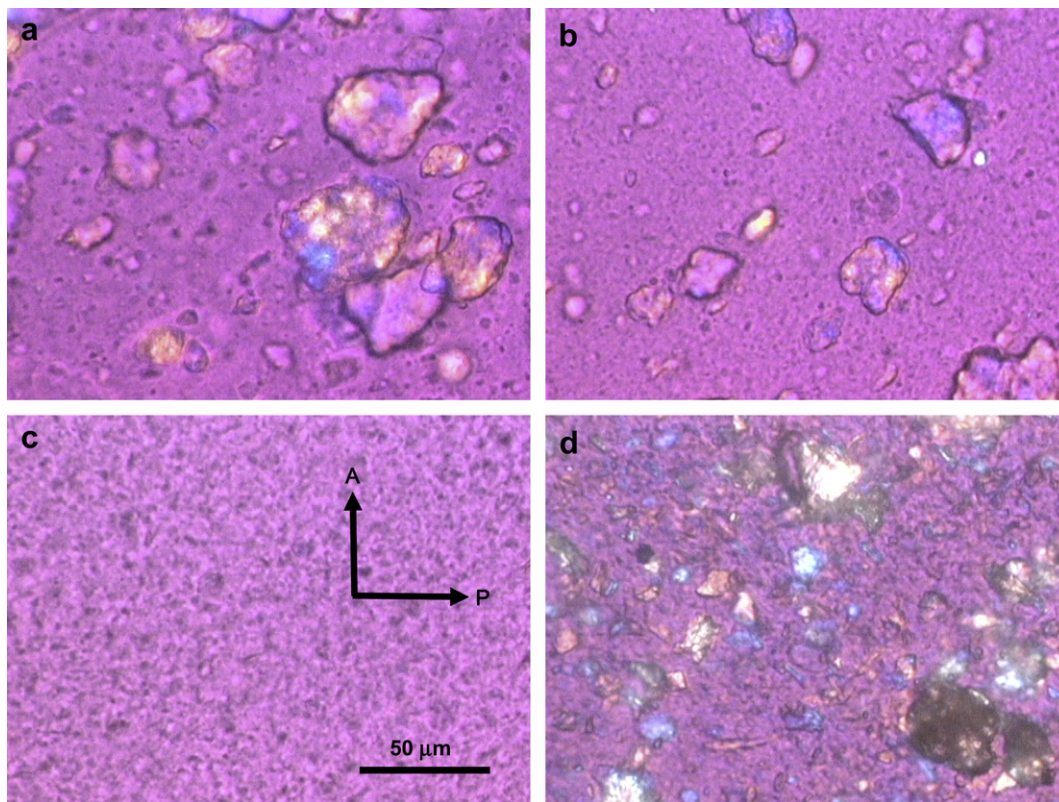


Fig. 1. Polarized optical micrographs of (a) PVDF/MMT-C₁₈TM, (b) PVDF/MMT-DC₁₈DM, (c) PVDF/syn-FH-DC₁₈DM, and (d) PVDF/HTO-C₁₈TM. All micrographs were taken at 200 °C just after annealing for 10 s.

nano-composite as well as PVDF/MMT systems. The internal structure of the nano-composites in the nanometer scale was directly observed via TEM analyses.

Fig. 2 shows the results of TEM bright field images of PVDF/HTO-C₁₈TM and PVDF/syn-FH-DC₁₈DM corresponding to the POM experiments, in which dark entities are the cross-section of layered

nano-fillers. The figure shows larger view permitting the observation of discrete nano-layers. The disorder and delaminated titanate layer structure is observed in PVDF/HTO-C₁₈TM. We estimated the form factors obtained from TEM images, i.e., average value of the particle length (L), thickness (D) of the dispersed particles and the correlation length (ξ) between the particles. The details of the

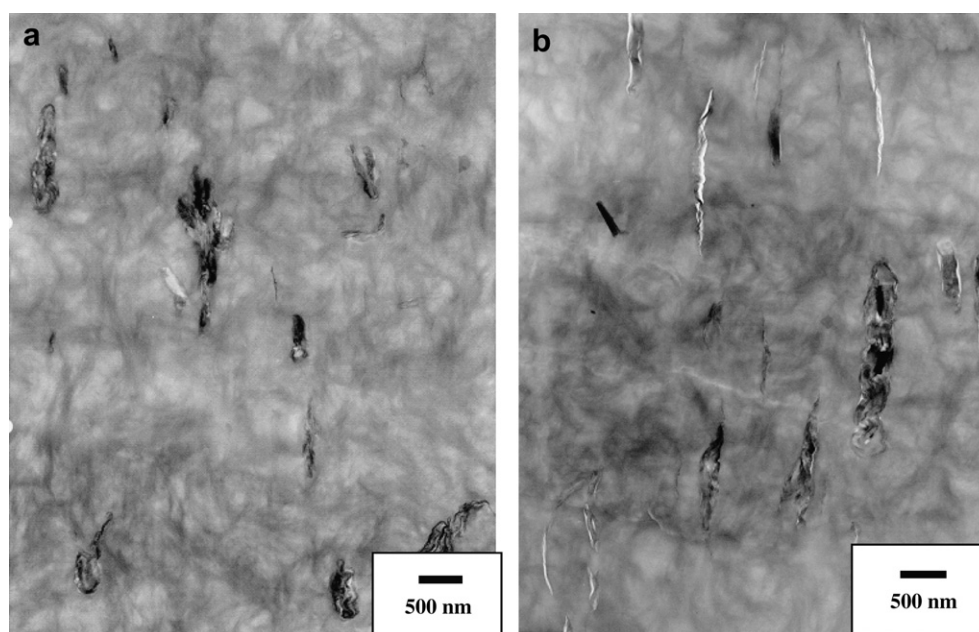


Fig. 2. Bright field TEM images of (a) PVDF/syn-FH-DC₁₈DM and (b) PVDF/HTO-C₁₈TM. The samples were crystallized at 150 °C after annealing at 200 °C for 3 min, and then cooled to room temperature. The dark entities are cross-section and/or face of intercalated-and-stacked silicate or titanate layers, and the bright areas are the matrix.

Table 4
Form factors of nano-composites obtained from WAXD and TEM observations

Nano-composites	PVDF/HTO-C ₁₈ TM	PVDF/syn-FH-DC ₁₈ DM
d_{001}/nm	2.74	3.13
D/nm	140 ± 19	90 ± 20
$(D/d_{001}) + 1$	60 ± 8	39 ± 8
L/nm	640 ± 104	900 ± 120
ξ/nm	940 ± 120	580 ± 53

evaluation were described in our previous paper [20]. The results are presented in Table 4. The mean interlayer spacing of the (001) plane ($d_{(001)}$) for the nano-composites is obtained by WAXD measurements. For PVDF/syn-FH-DC₁₈DM, D and L are in the range of (90 ± 20) nm and (900 ± 120) nm, respectively. On the other hand, PVDF/HTO-C₁₈TM exhibits large value of D (140 ± 19) nm, which is almost double the stacking of the nano-layers compared with that of PVDF/syn-FH-DC₁₈DM system. ξ value of the PVDF/syn-FH-DC₁₈DM (580 ± 53 nm) is lower than the value of PVDF/HTO-C₁₈TM (940 ± 120 nm), suggesting that the intercalated layers are more homogeneously and finely dispersed in case of PVDF/syn-FH-DC₁₈DM. The number of the stacked individual silicate layers ($\equiv D/d_{(001)} + 1$) is 39 ± 8 for PVDF/syn-FH-DC₁₈DM. The intercalated silicate layers are more homogeneously and finely dispersed as compared with titanate layers as revealed by POM observation.

In both systems, sharp peaks are observed at $2\theta \cong 2.82^\circ$ ($\cong 3.13$ nm) for PVDF/syn-FH-DC₁₈DM, and at $2\theta \cong 3.22^\circ$ ($\cong 2.74$ nm) for PVDF/HTO-C₁₈TM, corresponding to the (001) plane of the dispersed silicate and/or titanate layers in the PVDF matrix. The appearance of the (002) plane in both systems is also observed clearly. Note that the existence of sharp Bragg peak in PVDF-based nano-composites after melt mixing clearly indicates that the dispersed silicate and/or titanate layers still retain an ordered structure [19].

3.2. Crystalline structure

Fig. 3 shows WAXD profiles of neat PVDF and each nano-composite after crystallization at 130 and 150 °C for 4 h. The peaks are assigned as reported in the literature [25]. The neat PVDF exhibits a shoulder around $2\theta = 18.0^\circ$ due to diffraction from (100) plane, very strong reflections at $2\theta = 18.5^\circ$ and 20.1° due to diffraction from (020) and (110) planes, and another reflection peak at $2\theta = 26.88^\circ$ occurring from (021) plane. This peak well overlaps with the diffraction from (120) plane, which appears at $2\theta = 25.74^\circ$. These profiles indicate that neat PVDF crystals are the typical monoclinic unit cell (α -phase).

On the contrary, PVDF/MMTs and syn-FH-base nano-composite (PVDF/syn-FH) always exhibit predominantly a β - and/or γ -phase in the T_c range studied here. The diffraction peak at $2\theta = 20.54^\circ$ corresponds to the planes of (200)/(110) in β - and/or γ -phase, however, it is difficult to distinguish from each other due to the overlapping in the WAXD profile. This will be discussed in FTIR analysis.

Interestingly, at low T_c ($=110$ – 130 °C) PVDF/HTO system exhibits α -form and the fraction of γ -phase coexists with β -phase consistently increases with increasing T_c (see Fig. 4). Thus, the formation of the γ - and/or β -phase is enhanced in the presence of OMLF particles.

3.3. Temperature dependence of crystalline structure in PVDF/HTO system

As mentioned before, an overlap effect of the diffraction peak between 20.1° ((110) planes in α -phase) and 20.54° ((200)/(110) planes in β - and/or γ -phase) makes the peak deconvolution more difficult to estimate the formation of γ -phase crystallite. The final

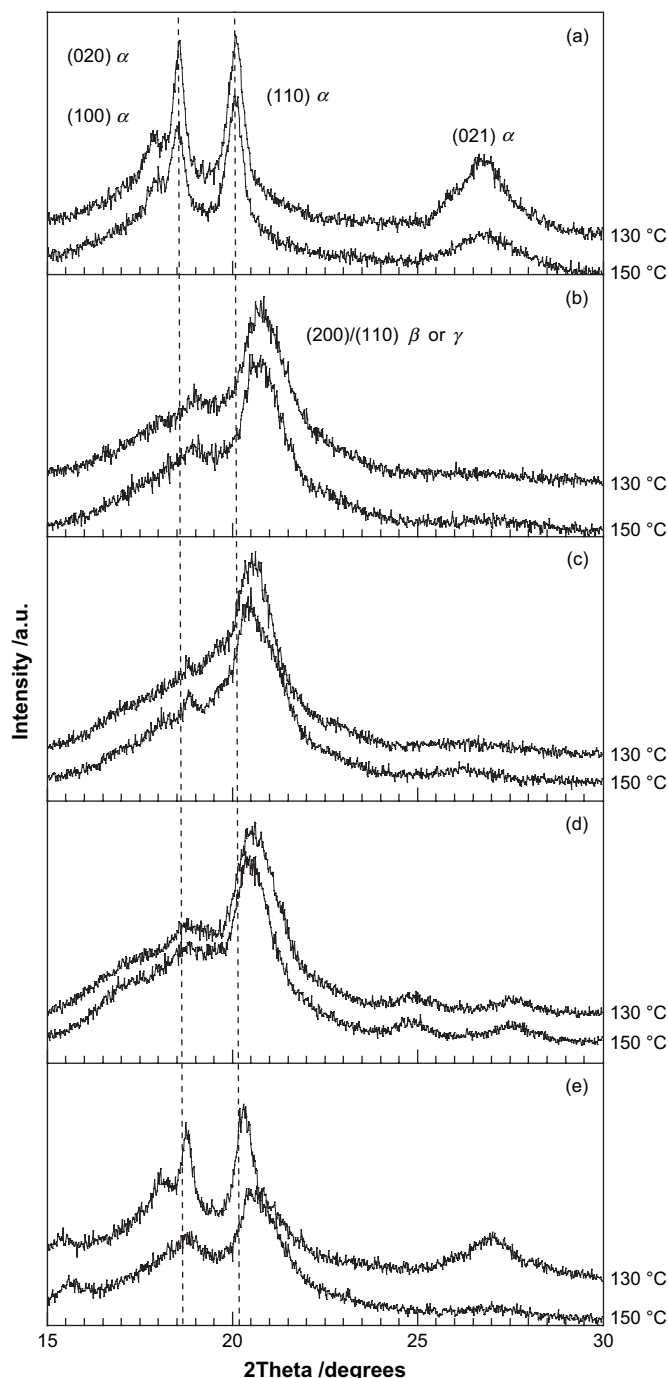


Fig. 3. WAXD profiles of (a) neat PVDF, (b) PVDF/MMT-C₁₈TM, (c) PVDF/MMT-DC₁₈DM, (d) PVDF/syn-FH-DC₁₈DM, and (e) PVDF/HTO-C₁₈TM. The samples were crystallized at 150 °C after annealing at 200 °C for 3 min, and then cooled to room temperature. All profiles were taken at room temperature.

crystallized samples are kept at room temperature and then subjected to the WAXD analyses. Therefore, the specimen involves β -phase crystallite due to the internal crystalline structure development during cooling from T_c [13].

For this reason, we have employed FTIR in order to distinguish the different crystallites.

Fig. 4 shows the spectral variations of neat PVDF and HTO-based nano-composite (PVDF/HTO) in the region of 1350 – 550 cm^{-1} during isothermal crystallization at 110 – 150 °C. Many crystalline-sensitive bands, which have been assigned for a regular repetition of *trans* (T) and *gauche* (G) conformations of the skeletal C–C bonds

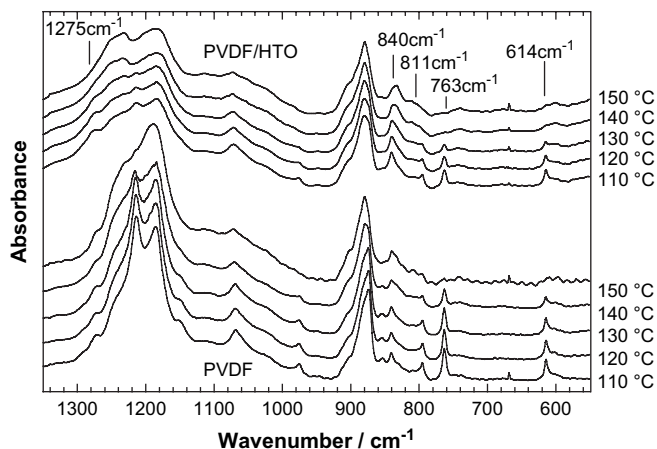


Fig. 4. Temperature dependence of infrared spectra for neat PVDF and PVDF/HTO. All spectra were taken at each T_c after isothermal crystallization in a heating chamber. The data in the y-axis direction were shifted to avoid the data overlap.

[26], are located in this region. Bands located at 1275, 840 cm^{-1} arise from the CF_2 asymmetric and symmetric stretchings, respectively. The skeletal C–C stretching vibration is also observed at 840 cm^{-1} . The appearance of these peaks is consistent with the conformational assignment of all-*trans* (long *trans* sequences) (*TTTTT*), as characteristic of β -phase. The band at 811 cm^{-1} is attributed to the CH_2 rocking mode in γ -phase (i.e., the formation of T_3G sequences: $T_3GT_3\bar{G}$). The weak intensity of bands at 763 cm^{-1} is due to the G band characteristic of α -phase. The band at 614 cm^{-1} is CF_2 bending mode, which is common to α - and γ -phase crystallites. Therefore, this band corresponds to *gauche* (*TG*) sequences.

Fig. 5 shows the crystallization temperature dependence of the characteristic bands and T_m obtained from DSC analysis. The absorbance of the 877 cm^{-1} band is regarded as an internal standard as reported by Tashiro et al. [26]. Therefore, the intensity ratio of crystalline-sensitive bands and the internal standard is used to depict the crystalline structure development.

The nano-composite (PVDF/HTO) exhibits the long *trans* sequence (1275 cm^{-1}), whose intensity decreases with the increase of T_c , at the same time, the band of 840 cm^{-1} decreases gradually.

For neat PVDF, the intensities of 1275 and 840 cm^{-1} do not change and remain small value (~ 0.15 for 1275 cm^{-1} and ~ 0.04 for 840 cm^{-1}) as compared with those of the nano-composite. For the nano-composite, the bands (763 and 614 cm^{-1}) decrease steadily, whereas both intensities of neat PVDF slightly increase to reach $T_c = 130$ °C and then decrease rapidly until T_c reaches 150 °C. The band of 811 cm^{-1} for PVDF/HTO remains constant value with the increase of T_c . Meanwhile, the intensity of neat PVDF (811 cm^{-1}) does not change and remain very small value (~ 0.005) at 150 °C. That is, the neat PVDF does not exhibit γ -phase in the temperature range of 110–130 °C. For this reason, it can be clearly seen that T_m shows almost same value (158–160 °C) compared with PVDF/HTO. The neat PVDF predominantly forms α -phase despite of the small evolution of the long *trans* sequence (β -phase) in the molecular conformation as seen in FTIR spectra.

On the other hand, for PVDF/HTO, the formation of T_3G sequences (811 cm^{-1}) takes place with the increase of T_c as compared with that of neat PVDF. We see that for PVDF/HTO the T_m at low T_c is almost constant (~ 157 °C) until $T_c = 135$ °C beyond which it increases abruptly to reach $T_m = 168.3$ °C at $T_c = 150$ °C due to the γ -phase formation of PVDF [27].

PVDF/HTO exhibits mainly α -phase crystal coexists with γ - and β -phases at low T_c range (110–135 °C). A major γ -phase crystal coexists with β - and α -phases is formed at high T_c ($=140$ – 150 °C), owing to the dispersed layer titanate particles, as revealed by

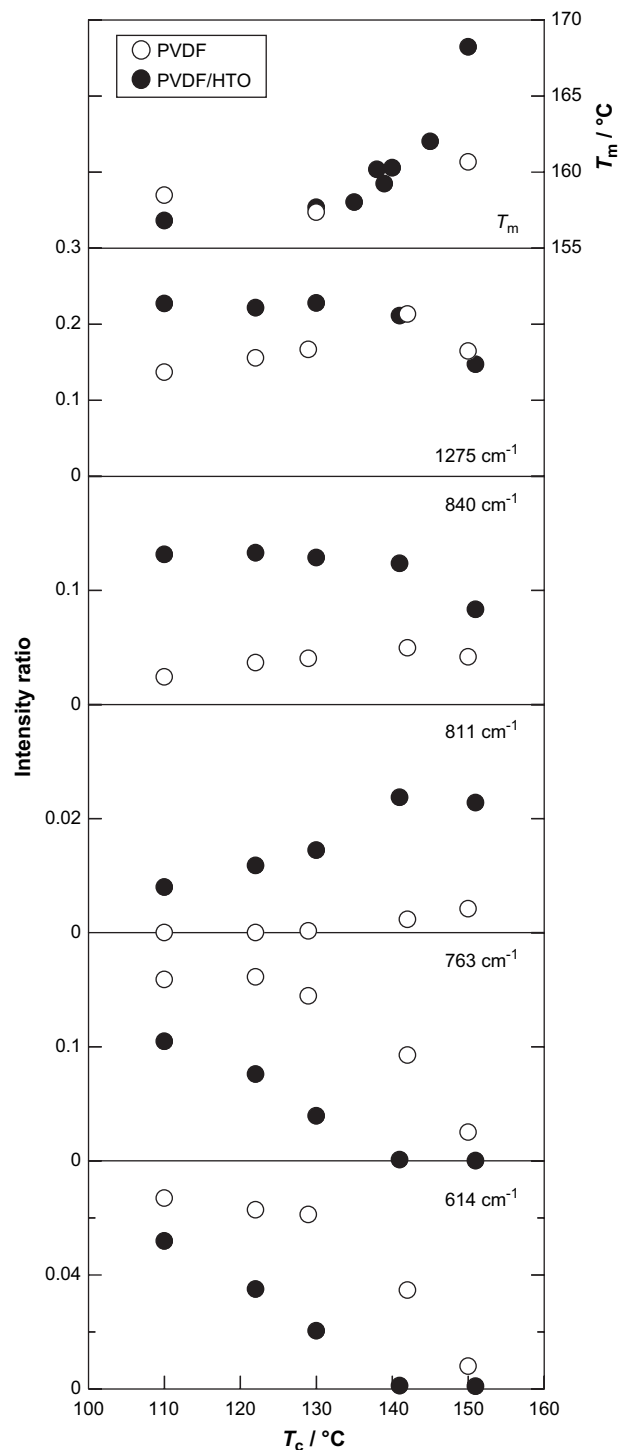


Fig. 5. T_c dependence of intensity ratio of crystalline-sensitive bands and T_m for neat PVDF and PVDF/HTO.

WAXD, DSC and FTIR analyses. The planes of (200)/(110) in β - and γ -phases strongly appear in the major WAXD peaks crystallized at 150 °C (see Fig. 4).

In PVDF/HTO, PVDF crystallized in the β - and γ -phases was irreversible at room temperature. The fact that the formation of the major γ -phase crystal at high T_c range in PVDF/HTO implies that the dispersed HTO- C_{18}TM particles induce epitaxially crystallized chain growth on their surfaces as a nucleating agent. Furthermore, partial removal of the intercalant (e.g., thermal degradation) offers a chance for the macromolecules to interact with HTO surface and

improve the nucleation effect. Apparently 5 wt% HTO–C₁₈TM is sufficient to nucleate the whole bulk and as a result the spherulitic pattern disappears but system crystallizes very quickly. The measurement of linear growth rate is impossible for PVDF/HTO by using POM observation.

3.4. Crystallization rate determined from light scattering

To understand the crystallization kinetics of neat PVDF and PVDF/HTO, we have used time-resolved LS photometry, which is a powerful tool for estimating the overall crystallization rate and its kinetics in supercooled crystalline polymer liquid [23]. For the kinetics of crystallization, we can employ the integrated scattering intensity, i.e., the invariant Q is define as

$$Q = \int_0^\infty I(q)q^2 dq \quad (2)$$

where q (scattering vector $= (4\pi/\lambda_{LS})\sin(\theta_{LS}/2)$) and $I(q)$ is the intensity of the scattered light at q [28].

In the H_V mode the invariant Q_δ can be described by the mean-square optical anisotropy $\langle \delta^2 \rangle$:

$$Q_\delta \propto \langle \delta^2 \rangle \propto \phi_s (\alpha_r - \alpha_t)^2 \quad (3)$$

where ϕ_s is the volume fraction of spherulites, and α_r and α_t are the radial and tangential polarizabilities of spherulites, respectively. We constructed a plot of reduced invariant Q_δ/Q_δ^∞ versus time t with Q_δ^∞ being Q_δ at an infinitely long time of crystallization (up to full solidification of the melt).

Fig. 6 shows the time variation of the invariant Q_δ/Q_δ^∞ taken for neat PVDF and PVDF/HTO at 130 °C. From the onset time t_0 we can estimate the induction time of the crystallization until start of crystallization, and we plotted it in Fig. 7 against T_c . At all T_c s measured here the t_0 value for PVDF/HTO is lower than that of pure PVDF. In the changes in t_0 with T_c , the PVDF/HTO shows remarkably short time especially at high T_c ($=146$ °C), suggesting that the

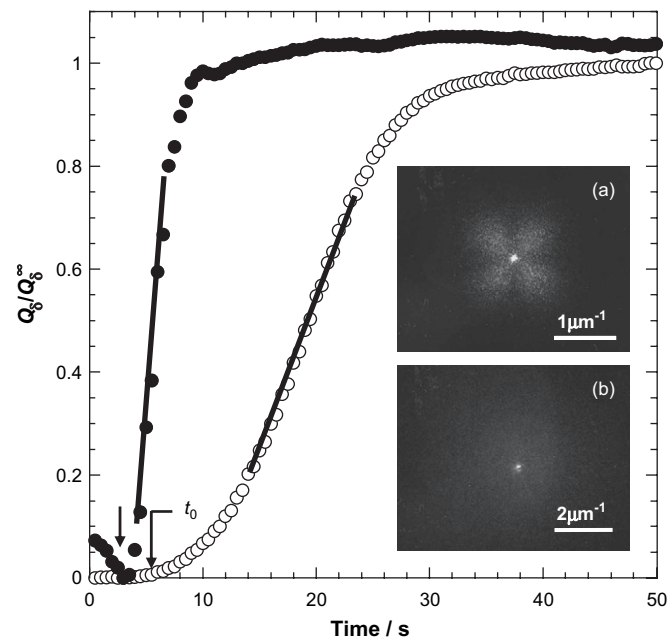


Fig. 6. Time variation of reduced invariant Q_δ/Q_δ^∞ during isothermal crystallization at quiescent state at $T_c = 130$ °C. The solid line represents the slope (overall crystallization rate). The arrows indicate the induction time of crystallization. The insets are the relevant H_V light scattering patterns after full solidification at $T_c = 130$ °C for (a) neat PVDF and (b) PVDF/HTO.

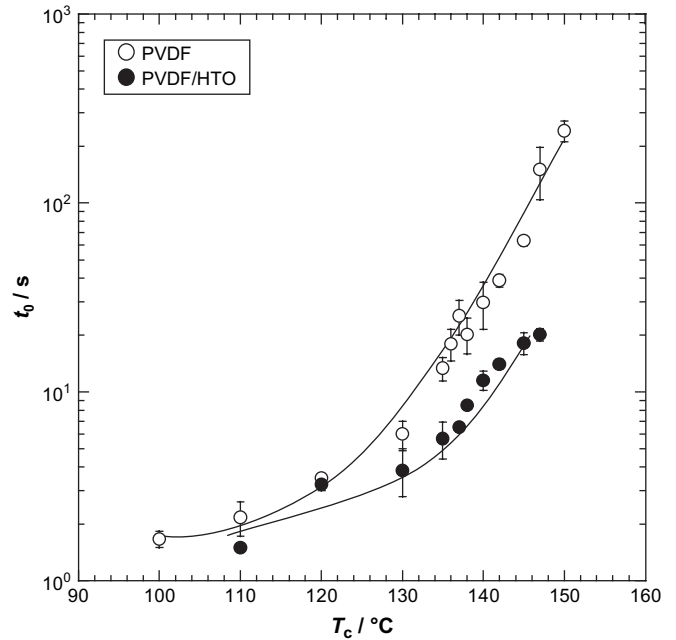


Fig. 7. T_c dependence of induction time for neat PVDF and PVDF/HTO.

dispersed nano-filler particles have some contribution to enhance the nucleation. As seen in Table 3, the higher T_{cc} value for these systems (PVDF/HTO, PVDF/MMT and PVDF/syn-FH) suggests that the systems are more easily crystallizable as compared with neat PVDF ($T_{cc} = \sim 128$ °C) during the DSC cooling process.

The overall crystallization rate was determined from the slope Q_δ/Q_δ^∞ ($d(Q_\delta/Q_\delta^\infty)/dt$) in the crystallization region as indicated by the solid line in Fig. 6. It is clear that the overall crystallization rate increases in PVDF/HTO, in comparison to the neat PVDF. The same trend is also observed over the wide range of T_c studied here.

In order to compare the crystallization rate, we assume heterogeneous nucleation and apply the Hoffman–Lauritzen growth rate equation slow kinetics [29,30] even if we are not using the analysis to determine linear growth rates. The growth rate of crystal can be written as

$$\text{Overall rate} \propto \beta_g \exp \left[-\frac{K_g}{T_c(\Delta T)f} \right] \quad (4)$$

where β_g is a mobility term, which describes the transportation rate of crystallizable molecules to the growth front; ΔT is the supercooling ($\equiv T_m^0 - T_c$, T_m^0 being equilibrium melting temperature); f is the correction factor given by $2T_c/(T_m^0 + T_c)$; and K_g is the nucleation constant, which depends on the crystallization regime (regime I, single nucleation; regimes II and III, multiple nucleation) [29,31]. The value of K_g in regimes I and III is twice that in regime II. At small undercoolings and over limited temperature range, the temperature dependence of growth is determined predominantly by the nucleation term. Accordingly, assuming that the $(d(Q_\delta/Q_\delta^\infty)/dt)$ is a satisfactory measure to the rate of crystallization, we plot the data as $(d(Q_\delta/Q_\delta^\infty)/dt)$ versus $1/(T_c\Delta T f)$: see Fig. 8.

The value of T_m^0 can be determined by Hoffman–Weeks [32] extrapolation based on plotting T_m against T_c . As seen in Fig. 9, we see quite a different behavior in PVDF/HTO between 130–140 °C range and the 145–150 °C range. In the 130–140 °C annealing (isothermal crystallization), the estimated value of T_m^0 by extrapolation is 163.6 °C, which is nicely conform to a value of the crystallized neat PVDF. Above 145 °C annealing the formation of γ -phase prevails as discussed in FTIR analysis. For this reason, the value of T_m^0 used is 163.6 °C for both neat PVDF and PVDF/HTO as measured by carrying out a Hoffman–Weeks plot as shown in Fig. 9.

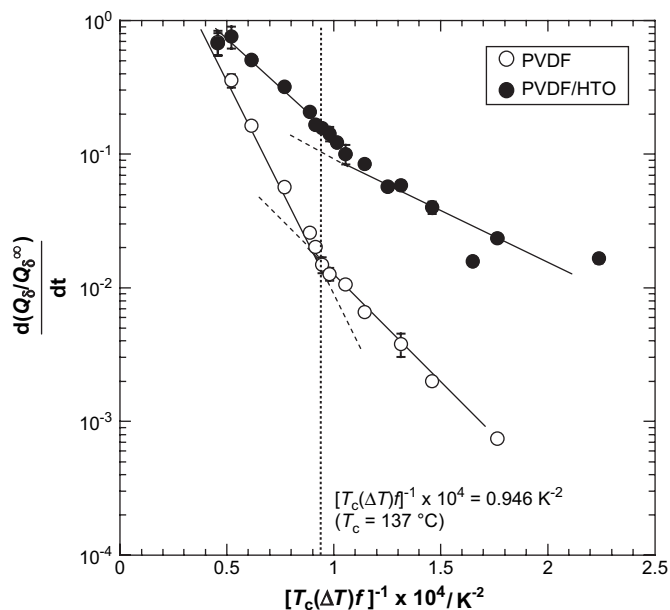


Fig. 8. The plot of overall crystallization rate versus $1/(T_c \Delta T f)$ for different T_c s in neat PVDF and PVDF/HTO. The broken line indicates $1/(T_c \Delta T f) = 0.946 \times 10^{-4} \text{ K}^{-2}$ ($T_c = 137 \text{ }^\circ\text{C}$).

The overall rate of PVDF/HTO is enhanced for every temperature of measurement, especially at higher T_c s. For neat PVDF crystallization, a change in slope at $1/(T_c \Delta T f) \approx 0.946 \times 10^{-4} \text{ K}^{-2}$ corresponding to $\Delta T \approx 26.6 \text{ }^\circ\text{C}$ ($T_c \approx 137 \text{ }^\circ\text{C}$) is obvious. The ratio of the two slopes is about 2, suggesting a transition from regime III to regime II at $T_c \approx 137 \text{ }^\circ\text{C}$. This feature is superficially similar to that Saito et al. found in their literature [33]. Similar change on undercooling is found for PVDF/HTO. The slope at low T_c ($=100\text{--}135 \text{ }^\circ\text{C}$) is almost twice of that at high T_c ($=140\text{--}153 \text{ }^\circ\text{C}$). Therefore it can be assumed that a transition occurs as the supercooling decreases and the system crystallized by regime II mechanism at $T_c > 137 \text{ }^\circ\text{C}$.

Another interesting feature is the formation of γ -phase in regime II. In regime II, a potential of a small difference between

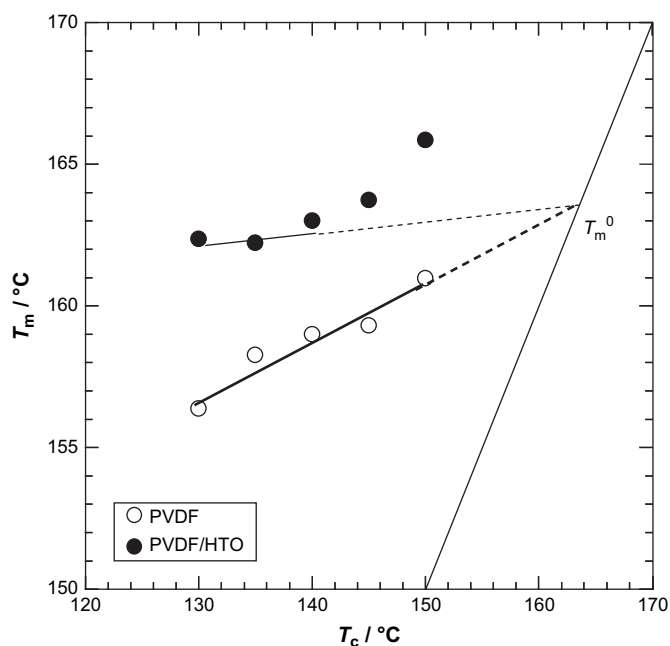


Fig. 9. Hoffman–Weeks plots for neat PVDF and PVDF/HTO crystallized isothermally at various temperatures.

secondary nucleation rate (i) and surface spreading rate (g) of the macromolecules on the dispersed titanate surfaces should be discussed in more detail. In regime III, the crystallization rate is mainly controlled by i , whereas, in regime II, both i and g prevail in the overall rate control. Therefore, it is speculated that the dispersed HTO particles induce epitaxially crystallized chain growth on their surfaces as a nucleating agent. The macromolecules to interact with HTO surface offer a chance for the formation of γ -phase in regime II. It should be realized that the nucleation effect in regime II (not regime III) is overwhelming.

3.5. Effect of the surface charge density of OMLFs

One more interesting feature is the surface charge density of OMLFs. How does the crystallization control by the surface charge density of the nano-fillers?

Both PVDF/MMT and PVDF/*syn*-FH exhibit the mixture of α -, β - and γ - phase crystalline structures at low T_c ($110\text{--}120 \text{ }^\circ\text{C}$). The major γ -phase crystal coexists with β - and α -phases is appeared at high T_c ($=130\text{--}150 \text{ }^\circ\text{C}$) as revealed by WAXD, DSC and FTIR analyses. A complete analysis of the results and more detailed data will be published later [34] (data not shown).

From these experimental results, for three nano-composites (PVDF/HTO, PVDF/MMT and PVDF/*syn*-FH), the similarities of the formation of γ -phase crystal at high T_c pointed out that the different polymorphs are not controlled by the surface charge density of the nano-fillers. However, at low T_c , three types of crystalline structure formation (i.e., α -, β - and γ -phases) are enhanced independently in the presence of OMLF particles having different charge densities.

As discussed in the beginning of this section, we could not employ LS photometry due to the big negative birefringence originated from the dispersed MMT and *syn*-FH nano-fillers in matrix PVDF as compared with that of well-crystallized neat PVDF. Unfortunately, we cannot discuss the crystallization kinetics in both PVDF/MMT and PVDF/*syn*-FH. Here we would like to note just experimental results for discussion in future. Such a discussion will be discussed separately [34].

4. Conclusions

We have prepared PVDF/organically modified layered titanate (HTO) nano-composite via melt intercalation technique. WAXD patterns and TEM observations established the formation of intercalated nano-composite. The detailed crystallization behavior and its kinetics of neat PVDF and nano-composite (PVDF/HTO) have been investigated.

The neat PVDF predominantly formed α -phase in the crystallization temperature range of $110\text{--}150 \text{ }^\circ\text{C}$ despite of the small evolution of the long *trans* sequence (β -phase) in the molecular conformation. On the other hand, PVDF/HTO exhibited mainly α -phase crystal coexisting with γ - and β -phases at low T_c range ($110\text{--}135 \text{ }^\circ\text{C}$). A major γ -phase crystal coexists with β - and α -phases appeared at high T_c ($=140\text{--}150 \text{ }^\circ\text{C}$), owing to the dispersed layer titanate particles, as revealed by WAXD, DSC and FTIR analyses. The overall crystallization rate on PVDF increased after nano-composite preparation with organically modified layered titanate. For both neat PVDF and PVDF/HTO crystallization, the transition from regime III to regime II was found to take place. It was speculated that the dispersed HTO particles induce epitaxially crystallized chain growth on their surfaces as a nucleating agent. The correlation between the formation of γ -phase in regime II and the macromolecules to interact with HTO surface was discussed.

Acknowledgment

This work was supported by the MEXT “Collaboration with Local Communities” Project (2005–2009).

References

- [1] Sinha Ray S, Okamoto M. *Prog Polym Sci* 2003;28:1539.
- [2] Vaia RA, Wagner HD. *Mater Today* 2004;7:32.
- [3] Gao F. *Mater Today* 2004;7:50.
- [4] Okamoto M. *Mater Sci Technol* 2006;22:756.
- [5] Okada A, Usuki A. *Macromol Mater Eng* 2006;291:1449.
- [6] Maiti P, Okamoto M. *Macromol Mater Eng* 2003;288:440.
- [7] Mathias L, Davis R, Jarrett W. *Macromolecules* 1999;32:7958.
- [8] Priya L, Jog JP. *J Polym Sci Part B Polym Phys* 2002;40:1682.
- [9] Priya L, Jog JP. *J Polym Sci Part B Polym Phys* 2003;41:31.
- [10] Priya L, Jog JP. *J Appl Polym Sci* 2003;89:2036.
- [11] Giannelis EP, Shah D, Maiti P, Gunn E, Schmidt DF, Jiang DD. *Adv Mater* 2004;16:1173.
- [12] Dillon DR, Tenneti KK, Li CY, Ko FK, Sics I, Hsiao BS. *Polymer* 2006;47:1678.
- [13] Buckley J, Cebe P, Cherdack D, Crawford J, Ince BS, Jenkins M, et al. *Polymer* 2006;47:2411.
- [14] Maiti P, Nam PH, Okamoto M, Kotaka T, Hasegawa N, Usuki A. *Macromolecules* 2002;35:2042.
- [15] Krikorian V, Pochan DJ. *Macromolecules* 2005;38:6520.
- [16] Nam JY, Sinha Ray S, Okamoto M. *Macromolecules* 2003;36:7126.
- [17] Hiroi R, Sinha Ray S, Okamoto M, Shiroy T. *Macromol Rapid Commun* 2004;25:1359.
- [18] Yoshida O, Okamoto M. *Macromol Rapid Commun* 2006;27:751.
- [19] Saito T, Okamoto M, Hiroi R, Yamamoto M, Shiroy T. *Polymer* 2007;48:4143.
- [20] Sinha Ray S, Yamada K, Okamoto M, Ogami A, Ueda K. *Chem Mater* 2003;15:1456.
- [21] Nam PH, Maiti P, Okamoto M, Kotaka T, Hasegawa N, Usuki A. *Polymer* 2001;42:9633.
- [22] Nakagawa K, Ishida Y. *J Polym Sci Part B Polym Phys* 1973;11:2153.
- [23] Kubo H, Sato H, Okamoto M, Kotaka T. *Polymer* 1998;39:501.
- [24] Greene KR. *Clay Miner* 1970;8:405.
- [25] Brandrup J, Immergut EH, Grulke EA, editors. *Polymer handbook*. 4th ed. New York: John Wiley & Sons; 1999.
- [26] Tashiro K, Kobayashi M, Tadokoro H. *Macromolecules* 1981;14:1757.
- [27] Nandi A, Mandelkern L. *J Polym Sci Part B Polym Phys* 1991;29:1287.
- [28] Okamoto M, Inoue T. *Polymer* 1995;36:2736.
- [29] Lauritzen JI, Hoffman JD. *J Appl Phys* 1973;44:4340.
- [30] Hoffman JD, Froln LJ, Ross GS, Lauritzen JI. *J Res Natl Bur Stand (A)* 1975;79:671.
- [31] Hoffman JD. *Polymer* 1983;24:3.
- [32] Martuscelli E, Silvestre S, Abate G. *Polymer* 1982;23:229.
- [33] Saito H, Okada T, Inoue T. *Macromolecules* 1991;24:4446.
- [34] Asai K, Okamoto M, Tashiro K. *Polymer*, submitted for publication.